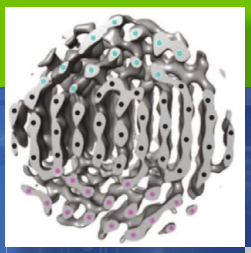

Atomic electron tomography in three and four dimensions

Jihan Zhou, Yongsoo Yang, Peter Ercius, and Jianwei Miao

Atomic electron tomography (AET) has become a powerful tool for atomic-scale structural characterization in three and four dimensions. It provides the ability to correlate structures and properties of materials at the single-atom level. With recent advances in data acquisition methods, iterative three-dimensional (3D) reconstruction algorithms, and post-processing methods, AET can now determine 3D atomic coordinates and chemical species with sub-Angstrom precision, and reveal their atomic-scale time evolution during dynamical processes. Here, we review the recent experimental and algorithmic developments of AET and highlight several groundbreaking experiments, which include pinpointing the 3D atom positions and chemical order/disorder in technologically relevant materials and capturing how atoms rearrange during early nucleation at four-dimensional atomic resolution.

Introduction

Recent years have witnessed an increasing demand for developing novel nanomaterials and nanostructures for applications in catalysis,[1–5] electronics,[6–8] energy conversion and storage,[9–11] quantum materials,[12–14] high-performance metals,[15–17] biosensing, and targeted delivery.[18–20] To customize and tailor functional properties, the three-dimensional (3D) atomic structures, including crystal defects and disorder, such as grain boundaries, dislocations, interfaces, and point defects, need to be determined. Furthermore, optimizing material synthesis and fabrication is essential for designing devices with desired properties. In order to achieve this, determination of just the 3D structure is not sufficient. Measuring atomic-scale dynamics during the sample fabrication process and under the working conditions of the device is a requirement.

Transmission electron microscopy (TEM) is routinely capable of imaging atomic structures, but only provides two-dimensional (2D) projection views of 3D crystalline samples. Scanning probe microscopy can image surface structures at atomic resolution, but not subsurface structures. Among several powerful 3D imaging and structural determination methods, including crystallography,[21,22] coherent diffractive imaging,[23–25] cryo-electron microscopy,[26–28] and atom probe tomography,[29,30] electron tomography has proven to be an important tool to image 3D structures of heterogeneous biological and physical samples with nanometer resolution.[31–33] By using crystallinity and other prior knowledge as constraints, electron tomography has been used to image the 3D structure of various nanostructures with atomic resolution from a single or a few projection images.[34–40] However, the specimen-specific constraints or crystallinity assumption make this technique not generally applicable to determine 3D crystal defects and disordered structures.

A major obstacle was overcome by the demonstration of atomic electron tomography (AET) in 2012, which achieved a 2.4 Å resolution without assuming crystallinity for the first time.[41] In 2015, AET was further advanced to determine the 3D coordinates of individual atoms in materials with 19 picometer precision.[42] The transformation from electron tomography at nanometer resolution[43–52] to AET capable of identifying 3D atomic positions in materials represents a quantum leap from qualitative to quantitative material characterization. Subsequently, AET has been applied to study crystal defects such as grain boundaries, dislocations, stacking faults, point defects, and strain tensors with unprecedented 3D detail.[41,42,53–56] The experimental atomic coordinates have also been used as direct input to *ab initio* calculations to correlate 3D atomic structures and the physical, chemical, and electronic properties of materials at the single-atom level.[55]

Jihan Zhou, Department of Physics and Astronomy, and California NanoSystems Institute, University of California, Los Angeles, USA; jihan.zhou@physics.ucla.edu
Yongsoo Yang, Department of Physics, Korea Advanced Institute of Science and Technology, Republic of Korea; yongsoo.yang@kaist.ac.kr
Peter Ercius, National Center for Electron Microscopy, Molecular Foundry Division, Lawrence Berkeley National Laboratory, USA; percius@lbl.gov
Jianwei Miao, Department of Physics and Astronomy, and California NanoSystems Institute, University of California, Los Angeles, USA; miao@physics.ucla.edu
doi:10.1557/mrs.2020.88

In this article, we review the experimental and computational aspects of AET, including data acquisition, image denoising and alignment, 3D image reconstruction, atom tracing, classification, and refinement. We illustrate recent developments in determining the 3D atomic coordinates and chemical order/disorder of nanomaterials. We also highlight the first experimental observation of early nucleation dynamics with four-dimensional (4D) AET (i.e., space + time).[56] Finally, we discuss the future challenges and opportunities of this powerful method for materials characterization in the 21st century.

Quantitative electron microscopy in three and four dimensions

Acquisition of tomographic tilt series

Electron tomography reconstructs 3D structural information from a tilt series of 2D electron microscope images acquired at many different viewing angles.[33,57–60] The resolution of an electron tomography reconstruction is set by the tilt range, the number of tilt angles, the electron dose applied to the sample, and the resolution of 2D projected images. Much effort has been employed to improve the resolution limit and stability of electron microscopy since its invention,[61–63] and aberration-corrected electron microscopy can now routinely achieve sub-Angstrom resolution with greater image contrast.[64]

Although AET was first demonstrated in conventional electron microscopy,[41,54] aberration-corrected electron microscopy has significantly facilitated data acquisition for AET. To reduce the diffraction contrast and multiple scattering effects, annular dark-field scanning transmission electron microscopy (ADF-STEM) has been used to acquire tomographic tilt series. Sample damage is the main issue in data acquisition, hence the following approaches have been implemented to mitigate radiation damage: (1) choosing appropriate operating voltages, (2) depositing a thin protective layer (e.g., carbon film) over the specimen, (3) finding the maximum tolerable electron dose for a specific sample, (4) reducing unnecessary dose on a sample as much as possible, and (5) taking multiple images at each angle and then aligning them to improve the signal-to-noise ratio.

Image preprocessing

Before the AET reconstruction, proper image processing must be done to remove any undesired effects such as image distortion due to drift, scan coil distortion, and noise. Multiple images (typically 3–10) acquired at each tilt angle are used to estimate and correct the specimen drift.[42,55,56,65] Scanning coil related distortions are corrected by applying a nonlinear, microscope-specific correction matrix obtained by analyzing a reference specimen with known lattice parameters[42,55,56,66] The signal-to-noise ratio of each image is further improved by applying advanced denoising techniques.[67] Next, each tilt series is aligned to a common tilt axis using two approaches. Parallel to the tilt axis direction, the images are aligned to each other with subpixel accuracy by the common-line method, using the fact that aligned projections in Fourier space must intersect on a single common line.[68,69] Perpendicular to the tilt axis direction, the alignment is achieved by the center of mass (CoM) method.[41,42,54–56] The CoM of each image is located, and the image is shifted so that the CoM coincides with the origin. This procedure is repeated until all of the images are aligned. These methods have been successful for achieving high-accuracy alignment of electron tomography tilt series.[41,42,54–56]

Advanced iterative reconstruction algorithms

AET tilt series have two intrinsic issues: (1) The missing wedge problem (i.e., the tilt range beyond ±75° cannot usually be measured due to geometrical constraints),[58] and (2) a limited number of projection images due to radiation damage.[70] Conventional tomographic methods such as filtered (or weighted) back projection[33,71] cannot produce good quality reconstructions due to incomplete data. Over the years, several iterative algorithms have been developed to alleviate this incomplete data problem.[72–74] One method, termed GENeralized Fourier Iterative REconstruction (GENFIRE), has recently been proven effective in reconstructing a 3D atomic structure from a limited number of projections with a missing wedge.[55,56,75,76] GENFIRE first assembles a 3D reciprocal grid from experimental 2D projections using oversampling to increase the gridding accuracy. The algorithm then iterates on the 3D grid between real and reciprocal space to search for a global solution that is consistent with the measured data (reciprocal space) and general physical constraints such as positivity and support (real space). During this iteration process, unmeasured information can be successfully retrieved. The GENFIRE algorithm is described in **Figure 1**a.

Post-processing of reconstructions: Atom tracing, species classification, and refinement

The 3D atomic positions and species can be determined from reconstructions. Figure 1b shows a cross-sectional view of a typical AET reconstruction of an FePt nanoparticle. The positions of local maxima within the volume (as shown by dots in Figure 1b) represent the positions of each atom in the nanoparticle. By applying a local maxima tracing algorithm, the 3D atomic coordinates can be precisely determined.[42,55,56] Atoms with larger atomic number (Z) will show higher intensities than those with lower Z elements for ADF-STEM tomography. The chemical species of each traced atom are classified based on the relative intensity contrast between different chemical species known to exist in a sample. Figure 1b shows that there are local maxima with relatively stronger intensity (Pt atoms) and weaker intensity (Fe atoms). Figure 1c shows the histogram of 5 × 5 × 5 voxels integrated intensities from the reconstruction volume for all traced atoms. Two Gaussian-shaped peaks are observed with some overlap. Most of the atoms can be clearly classified as Fe or Pt atoms based on their intensity. However, there are some ambiguous atoms in the overlapping region that need to be further classified. To separate these ambiguous atoms, an unbiased atom classification method needs to be used.[55] By comparing the volume profile of every traced atom with the averaged volume profile of each chemical species, all atoms can be iteratively reclassified

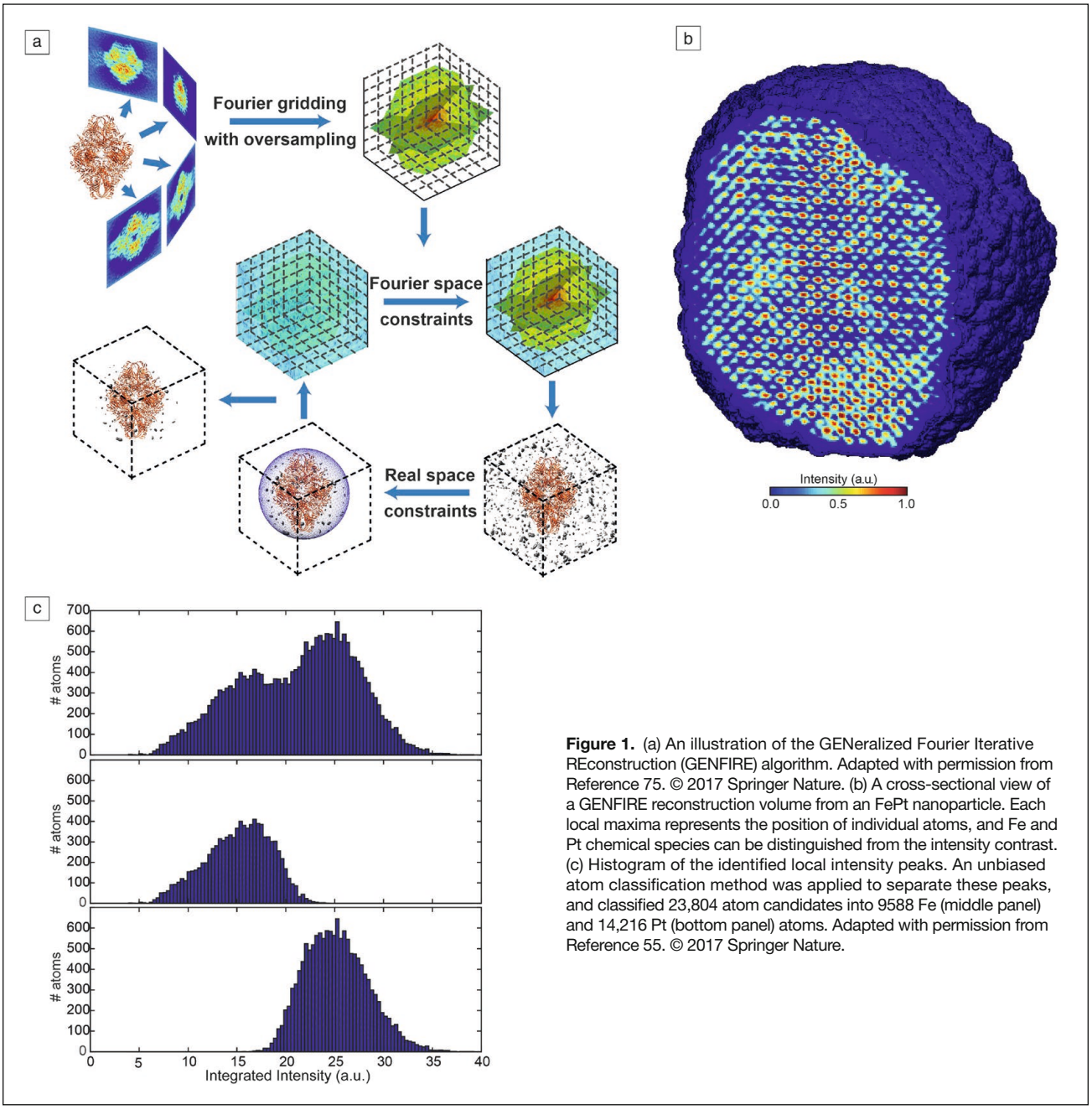

Figure 1. (a) An illustration of the GENeralized Fourier Iterative REconstruction (GENFIRE) algorithm. Adapted with permission from Reference 75. © 2017 Springer Nature. (b) A cross-sectional view of a GENFIRE reconstruction volume from an FePt nanoparticle. Each local maxima represents the position of individual atoms, and Fe and Pt chemical species can be distinguished from the intensity contrast. (c) Histogram of the identified local intensity peaks. An unbiased atom classification method was applied to separate these peaks, and classified 23,804 atom candidates into 9588 Fe (middle panel) and 14,216 Pt (bottom panel) atoms. Adapted with permission from Reference 55. © 2017 Springer Nature.

until a self-consistent average volume profile is reached. This method provides consistent classification results regardless of the initial starting configuration.[55,56] The obtained 3D atomic model (both atomic coordinates and chemical species) can be further refined by minimizing the error between the measured and simulated projections along the experimental tilt angles.[42,55,56]

Advances in atomic electron tomography

Three-dimensional atomic imaging of nanostructures

Three-dimensional atomic imaging of complex nanostructures with crystal defects such as grain boundaries, stacking faults, dislocations, and chemical order-disorder has been demonstrated with the acquisition of an atomically resolved tilt series and subsequent tomographic reconstruction. Scott et al. first demonstrated that AET can image a gold nanoparticle at 2.4 Å resolution without assuming crystallinity by combining ADF-STEM and an iterative reconstruction algorithm called equal slope tomography (EST) (**Figure 2**a).[41] The figure shows four major crystal grains, and individual atoms are observed in some regions in the nanoparticle. Chen et al. used a similar approach to study dislocations in a platinum nanoparticle by enhancing the signal-to-noise ratio of the reconstruction using 3D Fourier filtering.[54] Figure 2b shows a 5.3 Å-thick internal slice of the nanoparticle. A zigzag pattern, the characteristic feature of a screw dislocation core, is visible in the enlarged views.

https://doi.org/10.1557/mrs.2020.88

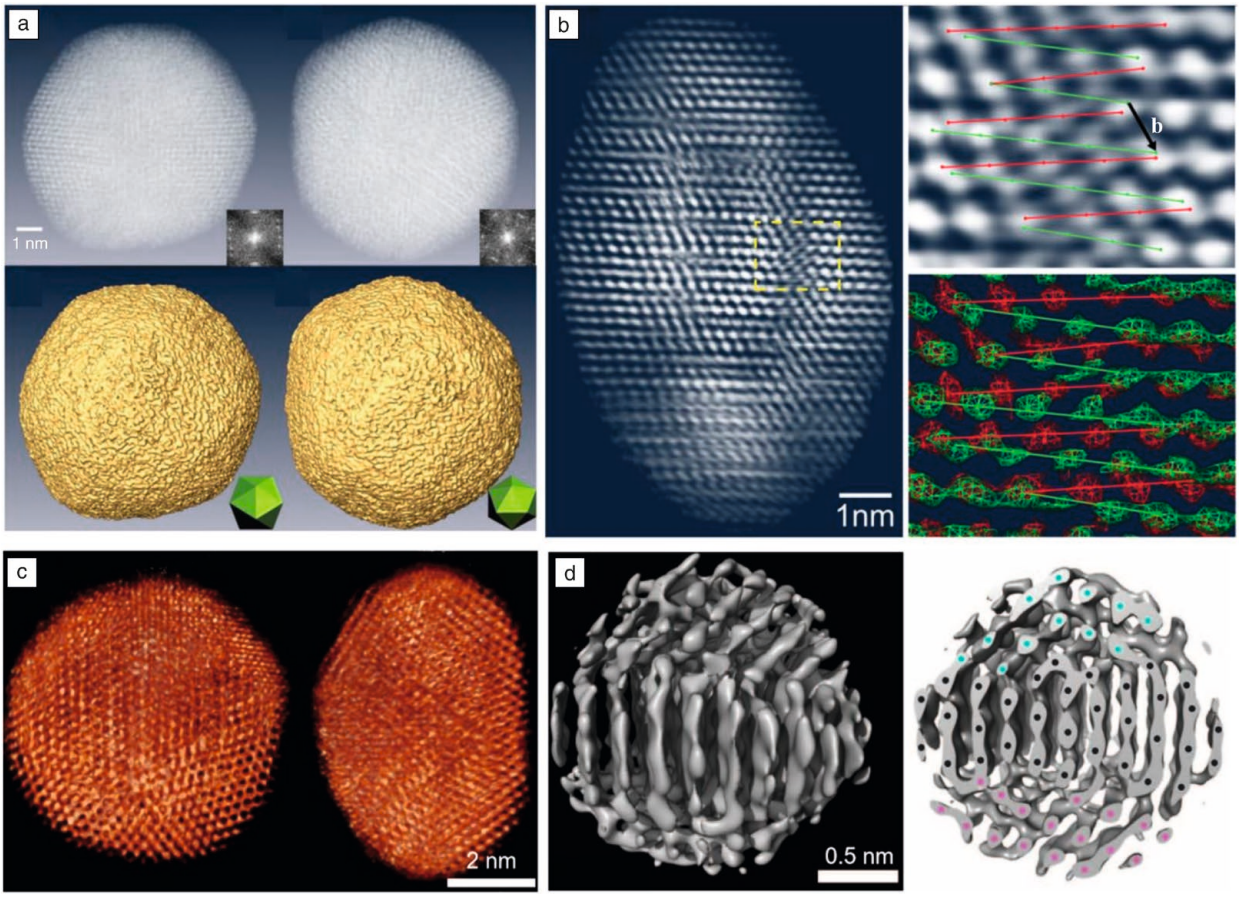

Figure 2. Three-dimensional (3D) atomic imaging of nanostructures using electron tomography. (a) Three-dimensional imaging of a gold nanoparticle at 2.4 Å resolution without assuming crystallinity or using averaging. Top shows the volume renderings of the 3D reconstruction of a gold nanoparticle and their Fourier transforms (insets) along the two- and threefold symmetry directions. Bottom shows the surface renderings of the 3D reconstruction with the inset icosahedron model along the same symmetry directions. Adapted with permission from Reference 41. © 2012 Springer Nature. (b) Three-dimensional imaging of dislocations in a platinum particle at atomic resolution. (Left) 5.3 Å thick internal slice (two atomic layers) of the nanoparticle reconstructed by atomic electron tomography. (Right, atoms are represented in green [top layer] and red dots [bottom layer]). Three-dimensional volume and surface renderings of an enlarged view of the core of a screw dislocation with the Burgers vector (b) of $\frac{1}{2}[01\bar{1}]$. Adapted with permission from Reference 54. © 2013 Springer Nature. (c) Three-dimensional reconstructions of a Ag-Au nanocluster. The volume-rendered 3D view shows atomic structure and composition of the cluster. Adapted from Reference 77. © 2015 Springer Nature. (d) Volume-rendered (left) and cross-sectional (right, the tentative atomic positions in each domain are represented in different colored dots. Views of the 3D structure of individual nanoparticles in liquid at near-atomic resolution. Adapted with permission from Reference 78. © 2015 AAAS.

Haberfehlner et al. demonstrated atomic resolution electron tomography of silver/gold core/shell nanoclusters using fewer numbers of projections and the simultaneous iterative reconstruction technique (SIRT) reconstruction algorithm.[77] From the reconstruction obtained by 31 STEM projections taken between 72° and –70°, the 3D morphology and composition of a cluster containing gold- and silver-rich regions can be identified without any prior information and with minimal filtering (Figure 2c). By searching for confined maxima, they found the atomic positions localized within the cluster volume. This 3D information provides insights into the growth and deposition process of the nanocluster.

Park et al. first determined the 3D structures of platinum nanocrystals in graphene liquid cells (ultrathin liquid containers made with one or two graphene sheets) at near-atomic resolution using the *ab initio* single-nanoparticle reconstruction method.[78] Figure 2d shows the 3D reconstruction of a Pt nanoparticle and the cross-sectional view along the vertical plane with tentative atomic positions indicated. This experiment demonstrates the ability to understand the structure and stability of nanocrystals in liquid.

Pinpointing atom locations and chemical order in three dimensions

Xu et al.[42] reported the first demonstration of precise (±19 pm precision) 3D atomic structural determination of thousands of individual atoms via AET. They measured the full atomic coordinates of 3769 atoms that formed the first nine atomic layers of a tungsten needle tip sample (**Figure 3**a). The atomic displacement field and the full 3D strain tensor was calculated

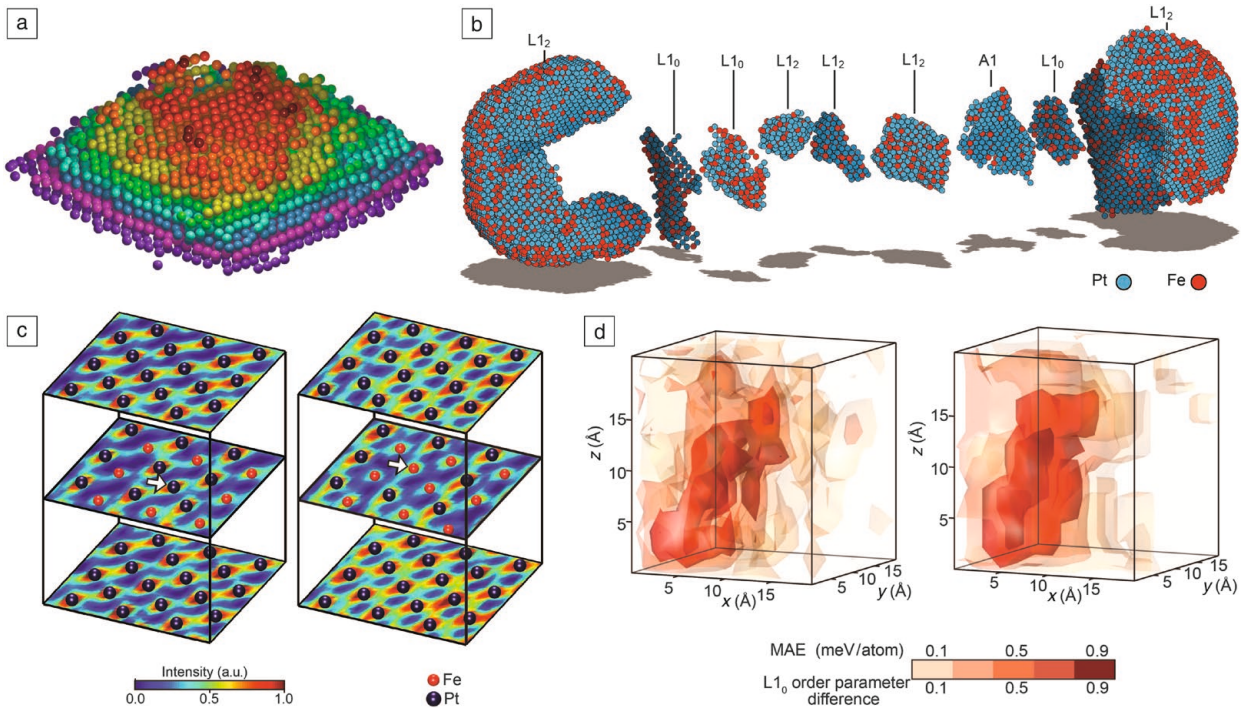

Figure 3. (a) Experimentally determined 3D positions of individual atoms in a tungsten needle sample revealed by electron tomography. The 3D atomic model of the sample consists of nine atomic layers along the [011] direction, colored dark red, red, orange, yellow, green, cyan, blue, magenta, and purple from layers 1–9, respectively. Adapted with permission from Reference 42. © 2015 Springer Nature. (b) Experimentally determined complex grain structure of an FePt nanoparticle via atomic electron tomography. The nanoparticle consists of two large $L1_2$ grains, three small $L1_2$ grains, three small $L1_0$ grains, and a Pt-rich A1 grain. (c) Three-dimensional atomic positions overlaid on the 3D reconstructed intensity (color scale at bottom) illustrating antisite point defects (arrows): a Pt atom occupying an Fe atom site (left), an Fe atom occupying a Pt atom site (right). (d) Three-dimensional isosurface rendering of the calculated local magnetocrystalline anisotropy energy (MAE, left) and $L1_0$ order parameter differences (right) obtained from an $L1_0$ ordered grain within the nanoparticle. Adapted with permission from Reference 55. © 2017 Springer Nature.

with a resolution of 1 nm^3 and a precision of 10^{-3}, respectively. Density functional theory (DFT) calculations and molecular dynamics simulations verified that the observed strain originates from the tungsten carbide formed at the surface of the tip and diffusion of carbon several layers inside the needle.[42]

Another important breakthrough has been made for measuring the chemical order/disorder atomic structure of transition-metal-based alloy compounds. Yang et al. applied AET to precisely determine the 3D coordinates (±22 pm precision) and chemical species (99% accuracy) of an FePt nanoparticle.[55] The internal chemically ordered grain structure was fully characterized. A rich structural variety of grain boundaries, antiphase boundaries, antisite point defects, and swap defects were observed (Figure 3b–c). The experimentally measured coordinates and chemical species were directly input to DFT calculations. The spin and orbital magnetic moments were successfully determined for individual atoms within an $L1_0$ phase grain, showing variations depending on local atomic coordinates and chemical ordering. Furthermore, local magnetocrystalline anisotropy energy (MAE), the main property of interest for magnetic device applications, can also be calculated, which showed direct correlation with the local order parameters (Figure 3d). This work demonstrated not only the capabilities of AET to precisely determine full 3D atomic coordinates and chemical species of complex nanomaterials, but also that AET can be combined with quantum mechanical calculations to reveal the physical properties at the atomic scale. This suggests a new way to understand structure–property relationships of functional materials.

Capturing atom motion in four dimensions

While the 3D static atomic structure of materials is important to understand their functionality, there is significant interest in revealing the structure and dynamics of materials at 4D atomic resolution to study processes such as nucleation and growth. Zhou et al. recently studied the dynamics of early-stage nucleation in an *ex situ* AET experiment (**Figure 4**) using FePt nanoparticles as a model system.[56] Selected FePt nanoparticles were first annealed at 520°C in a vacuum for nine minutes, and tilt series were measured at room temperature. Next, the nanoparticles were further annealed (520°C) and then measured at room temperature for 2–3 different annealing times. For all measured tilt series, 3D atomic models were obtained and analyzed using the same reconstruction method.

https://doi.org/10.1557/mrs.2020.88

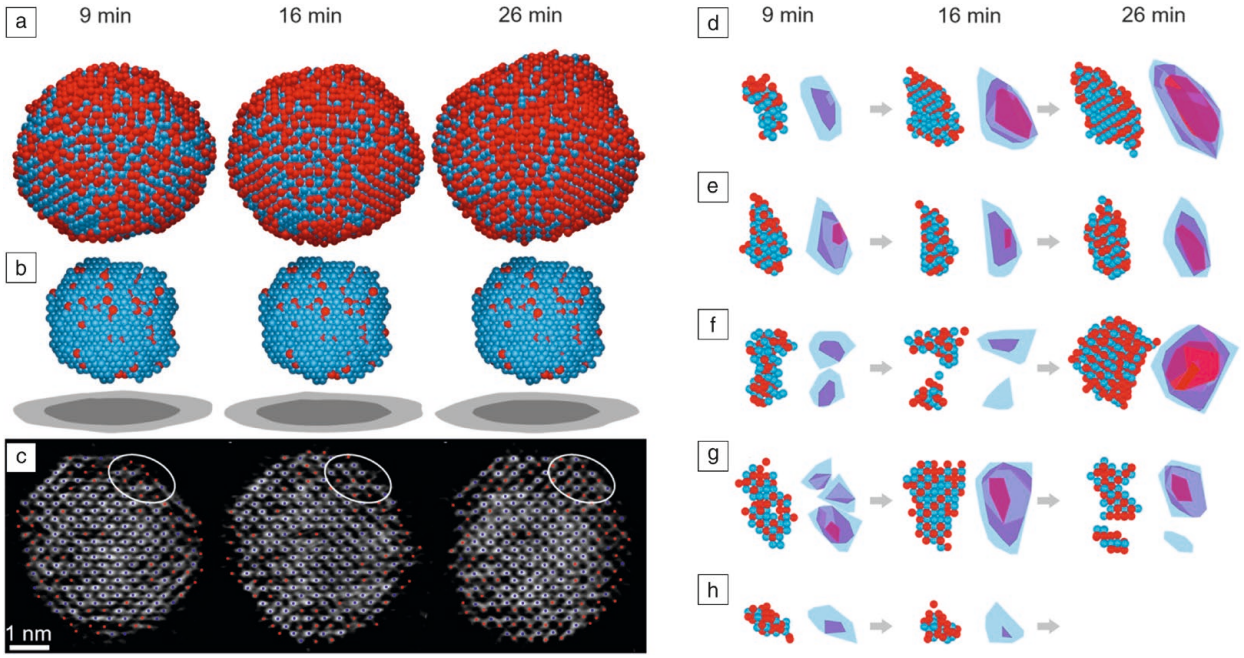

Figure 4. Capturing 4D atom motion with atomic electron tomography. (a) Three-dimensional (3D) atomic models (Fe in red and Pt in blue) of an FePt nanoparticle with an accumulated annealing time of 9 min, 16 min, and 26 min, respectively. (b) The Pt-rich core of the nanoparticle (shown here) remained the same for the three annealing times. The light and dark gray projections below the models show the whole nanoparticle and the core, respectively. (c) The same internal atomic layer of the nanoparticle along the [010] direction at the three annealing times, where a fraction of the surface and subsurface atoms had rearranged to form $L1_0$ phase (ellipses). (d) Representative growing, (e–g) fluctuating, and (h) dissolving nuclei with an accumulated annealing time of 9 min, 16 min, and 26 min, respectively. The atomic models show Fe (red) and Pt (blue) atoms with an order parameter ≥0.3, and the 3D contour maps show the distribution of an order parameter of 0.7 (red), 0.5 (purple), and 0.3 (light blue). Adapted with permission from Reference 56.

Figure 4a shows the atomic models of the same nanoparticle with an accumulated annealing time of 9 min, 16 min, and 26 min, respectively. The atoms on and near the surface rearrange to form $L1_0$ phases, while the Pt-rich core of the nanoparticle stays nearly the same (Figure 4b), which is evident when comparing the same internal atomic layers along the [010] direction (Figure 4c). By tracking the common nuclei in the particle, they found that early-stage nuclei were irregularly shaped—each had a core of one to a few atoms with the maximum order parameter—and the initiation of nucleation mainly occurred on the surface of the nanoparticles. The nuclei underwent growth (Figure 4d), fluctuation (Figure 4e–g), dissolution (Figure 4h), merging and division (Figure 4f–g), depending on the order parameter gradient distribution as well as thermodynamics and kinetics.

These results not only revealed a never-before-seen view of nucleation, but also indicated that a theory beyond classical nucleation theory is needed to describe early-stage nucleation at the atomic scale. This experiment adds a new dimension (time) to AET (i.e., 4D AET), capturing atomic motion in materials in four dimensions, which is currently not accessible by any other experimental methods. Four-dimensional AET could potentially serve as a powerful tool in studying many fundamental problems such as phase transitions, atomic diffusion, grain-boundary dynamics, interface motion, defect dynamics, and surface reconstruction.

Summary and outlook

With recent developments in electron microscopy, data analysis procedures, advanced iterative reconstruction algorithms, atom tracing, and refinement methods, AET has made several breakthroughs. We are now in the process of being able to precisely determine the 3D positions of individual atoms in materials and probing their dynamics at 4D atomic resolution. Several examples of AET in 3D and 4D were summarized in this article.

The future research frontiers of AET bring up more challenges and opportunities in solving fundamental problems such as disorder structures, electron-beam-sensitive structures, and *in situ* 3D atomic dynamics. Several novel techniques could be employed to further improve the capabilities of AET, such as ptychography,[79–81] atomic elemental mapping,[82,83] 4D-STEM,[84,85] dose-efficient STEM,[86] low-dose modality imaging schemes with either advanced direct electron detectors[87] or cryogen temperature environment,[88,89] and *in situ* atomic imaging microscopy.[90,91] On the algorithm and methods side, new methods,[92] new reconstruction algorithms,[93] and machine learning could further extend the applicability of AET to 2D materials, heterostructures, thin films, and other material systems. With a combination of novel imaging modes and advanced reconstruction algorithms, we anticipate that AET will play a key role in solving many fundamental problems

in materials science, nanoscience, condensed-matter physics, and chemistry.

Acknowledgments

This work was supported by STROBE, A National Science Foundation Science & Technology Center (DMR-1548924), the Office of Basic Energy Sciences of the US DOE (DE-SC0010378), an Army Research Office MURI Grant on *Ab Initio* Solid-State Quantum Materials: Design, Production and Characterization at the Atomic Scale (18057522), and the Division of Materials Research of the US NSF (DMR-1437263). P.E. is supported by the Molecular Foundry, Lawrence Berkeley National Laboratory, which is supported by the US Department of Energy under Contract No. DE-AC02–05CH11231. Y.Y. acknowledges support by the National Research Foundation of Korea (NRF) Grant funded by the Korean Government (MEST) (No. 2019R1F1A1058236).

References

1. V.R. Stamenkovic, B. Fowler, B.S. Mun, G. Wang, P.N. Ross, C.A. Lucas, N.M. Marković, *Science* **315**, 493 (2007).
2. Y. Ding, M. Chen, *MRS Bull.* **34**, 569 (2009).
3. B. Lim, M. Jiang, P.H.C. Camargo, E.C. Cho, J. Tao, X. Lu, Y. Zhu, Y. Xia, *Science* **324**, 1302 (2009).
4. X. Huang, Z. Zhao, L. Cao, Y. Chen, E. Zhu, Z. Lin, M. Li, A. Yan, A. Zettl, Y.M. Wang, X. Duan, T. Mueller, Y. Huang, *Science* **348**, 1230 (2015).
5. L. Lin, W. Zhou, R. Gao, S. Yao, X. Zhang, W. Xu, S. Zheng, Z. Jiang, Q. Yu, Y.-W. Li, C. Shi, X.-D. Wen, D. Ma, *Nature* **544**, 80 (2017).
6. M. Law, J. Goldberger, P. Yang, *Annu. Rev. Mater. Res.* **34**, 83 (2004).
7. B. Tian, X. Zheng, T.J. Kempa, Y. Fang, N. Yu, G. Yu, J. Huang, C.M. Lieber, *Nature* **449**, 885 (2007).
8. L. Dou, A.B. Wong, Y. Yu, M. Lai, N. Kornienko, S.W. Eaton, A. Fu, C.G. Bischak, J. Ma, T. Ding, N.S. Ginsberg, L.-W. Wang, A.P. Alivisatos, P. Yang, *Science* **349**, 1518 (2015).
9. A.S. Aricò, P. Bruce, B. Scrosati, J.-M. Tarascon, W. van Schalkwijk, *Nat. Mater.* **4**, 366 (2005).
10. B. Kang, G. Ceder, *Nature* **458**, 190 (2009).
11. H. Sun, J. Zhu, D. Baumann, L. Peng, Y. Xu, I. Shakir, Y. Huang, X. Duan, *Nat. Rev. Mater.* **4**, 45 (2019).
12. X. Qian, J. Liu, L. Fu, J. Li, *Science* **346**, 1344 (2014).
13. P. Liu, J.R. Williams, J.J. Cha, *Nat. Rev. Mater.* **4**, 479 (2019).
14. X. Liu, M.C. Hersam, *Nat. Rev. Mater.* **4**, 669 (2019).
15. Y. Wang, M. Chen, F. Zhou, E. Ma, *Nature* **419**, 912 (2002).
16. B. Gludovatz, A. Hohenwarter, D. Catoor, E.H. Chang, E.P. George, R.O. Ritchie, *Science* **345**, 1153 (2014).
17. E. Lilleodden, P. Voorhees, *MRS Bull.* **43**, 20 (2018).
18. N.L. Rosi, C.A. Mirkin, *Chem. Rev.* **105**, 1547 (2005).
19. P.D. Howes, R. Chandrawati, M.M. Stevens, *Science* **346**, 1247390 (2014).
20. Y. Ding, Z. Jiang, K. Saha, C.S. Kim, S.T. Kim, R.F. Landis, V.M. Rotello, *Mol. Ther.* **22**, 1075 (2014).
21. M. Ladd, R. Palmer, *Structure Determination by X-Ray Crystallography* (Plenum Press, New York, 1994).
22. J. Drenth, *Principles of Protein X-Ray Crystallography* (Springer, New York, 1994).
23. J. Miao, P. Charalambous, J. Kirz, D. Sayre, *Nature* **400**, 342 (1999).
24. I. Robinson, R. Harder, *Nat. Mater.* **8**, 291 (2009).
25. J. Miao, T. Ishikawa, I.K. Robinson, M.M. Murnane, *Science* **348**, 530 (2015).
26. Y. Cheng, *Cell* **161**, 450 (2015).
27. E. Nogales, *Nat. Methods* **13**, 24 (2016).
28. P. Zhang, *Curr. Opin. Struct. Biol.* **58**, 249 (2019).
29. T.F. Kelly, M.K. Miller, *Rev. Sci. Instrum.* **78**, 031101 (2007).
30. D. Seidman, K. Stiller, *MRS Bull.* **34**, 717 (2009).
31. D.J. de Rosier, A. Klug, *Nature* **217**, 130 (1968).
32. R.G. Hart, *Science* **159**, 1464 (1968).
33. J. Frank, *Electron Tomography: Methods for Three-DimensionalVisualization of Structures in the Cell* (Springer, New York, 2010).
34. Z.Y. Li, N.P. Young, M. Di Vece, S. Palomba, R.E. Palmer, A.L. Bleloch, B.C. Curley, R.L. Johnston, J. Jiang, J. Yuan, *Nature* **451**, 46 (2008).
35. S. Van Aert, K.J. Batenburg, M.D. Rossell, R. Erni, G. Van Tendeloo, *Nature* **470**, 374 (2011).
36. B. Goris, S. Bals, W. Van den Broek, E. Carbó-Argibay, S. Gómez-Graña, L.M. Liz-Marzán, G. Van Tendeloo, *Nat. Mater.* **11**, 930 (2012).
37. D. Van Dyck, J.R. Jinschek, F.-R. Chen, *Nature* **486**, 243 (2012).
38. J. Hwang, J.Y. Zhang, A.J. D'Alfonso, L.J. Allen, S. Stemmer, *Phys. Rev. Lett.* **111**, 266101 (2013).
39. M. Azubel, J. Koivisto, S. Malola, D. Bushnell, G.L. Hura, A.L. Koh, H. Tsunoyama, T. Tsukuda, M. Pettersson, H. Häkkinen, R.D. Kornberg, *Science* **345**, 909 (2014).
40. C.L. Jia, S.B. Mi, J. Barthel, D.W. Wang, R.E. Dunin-Borkowski, K.W. Urban, A. Thust, *Nat. Mater.* **13**, 1044 (2014).
41. M.C. Scott, C.-C. Chen, M. Mecklenburg, C. Zhu, R. Xu, P. Ercius, U. Dahmen, B.C. Regan, J. Miao, *Nature* **483**, 444 (2012).
42. R. Xu, C.-C. Chen, L. Wu, M.C. Scott, W. Theis, C. Ophus, M. Bartels, Y. Yang, H. Ramezani-Dakhel, M.R. Sawaya, H. Heinz, L.D. Marks, P. Ercius, J. Miao, *Nat. Mater.* **14**, 1099 (2015).
43. P.A. Midgley, M. Weyland, *Ultramicroscopy* **96**, 413 (2003).
44. P.A. Midgley, J.M. Thomas, L. Laffont, M. Weyland, R. Raja, B.F.G. Johnson, T. Khimyak, *J. Phys. Chem. B* **108**, 4590 (2004).
45. I. Arslan, T.J.V. Yates, N.D. Browning, P.A. Midgley, *Science* **309**, 2195 (2005).
46. P. Ercius, M. Weyland, D.A. Muller, L.M. Gignac, *Appl. Phys. Lett.* **88**, 243116 (2006).
47. S. Bals, K.J. Batenburg, J. Verbeeck, J. Sijbers, G. Van Tendeloo, *Nano Lett.* **7**, 3669 (2007).
48. E.P.W. Ward, T.J.V. Yates, J.-J. Fernández, D.E.W. Vaughan, P.A. Midgley, *J. Phys. Chem. C* **111**, 11501 (2007).
49. T. Yaguchi, M. Konno, T. Kamino, M. Watanabe, *Ultramicroscopy* **108**, 1603 (2008).
50. H.L. Xin, P. Ercius, K.J. Hughes, J.R. Engstrom, D.A. Muller, *Appl. Phys. Lett.* **96**, 223108 (2010).
51. A. Genc, L. Kovarik, M. Gu, H. Cheng, P. Plachinda, L. Pullan, B. Freitag, C. Wang, *Ultramicroscopy* **131**, 24 (2013).
52. J. Zhou, M. Taylor, G.A. Melinte, A.J. Shahani, C.C. Dharmawardhana, H. Heinz, P.W. Voorhees, J.H. Perepezko, K. Bustillo, P. Ercius, J. Miao, *Sci. Rep.* **8**, 10239 (2018).
53. J. Miao, P. Ercius, S.J.L. Billinge, *Science* **353**, aaf2157 (2016).
54. C.-C. Chen, C. Zhu, E.R. White, C.-Y. Chiu, M.C. Scott, B.C. Regan, L.D. Marks, Y. Huang, J. Miao, *Nature* **496**, 74 (2013).
55. Y. Yang, C.-C. Chen, M.C. Scott, C. Ophus, R. Xu, A. Pryor, L. Wu, F. Sun, W. Theis, J. Zhou, M. Eisenbach, P.R.C. Kent, R.F. Sabirianov, H. Zeng, P. Ercius, J. Miao, *Nature* **542**, 75 (2017).
56. J. Zhou, Y. Yang, Y. Yang, D.S. Kim, A. Yuan, X. Tian, C. Ophus, F. Sun, A.K. Schmid, M. Nathanson, H. Heinz, Q. An, H. Zeng, P. Ercius, J. Miao, *Nature* **570**, 500 (2019).
57. P.A. Midgley, E.P.W. Ward, A.B. Hungría, J.M. Thomas, *Chem. Soc. Rev.* **36**, 1477 (2007).
58. P.A. Midgley, R.E. Dunin-Borkowski, *Nat. Mater.* **8**, 271 (2009).
59. Z. Saghi, P.A. Midgley, *Annu. Rev. Mater. Res.* **42**, 59 (2012).
60. P. Ercius, O. Alaidi, M.J. Rames, G. Ren, *Adv. Mater.* **27**, 5638 (2015).
61. M. Haider, S. Uhlemann, E. Schwan, H. Rose, B. Kabius, K. Urban, *Nature* **392**, 768 (1998).
62. P.E. Batson, N. Dellby, O.L. Krivanek, *Nature* **418**, 617 (2002).
63. S.J. Pennycook, *Ultramicroscopy* **180**, 22 (2017).
64. R. Erni, M.D. Rossell, C. Kisielowski, U. Dahmen, *Phys. Rev. Lett.* **102**, 096101 (2009).
65. C. Ophus, J. Ciston, C.T. Nelson, *Ultramicroscopy* **162**, 1 (2016).
66. K.G. Larkin, M.A. Oldfield, H. Klemm, *Opt. Commun.* **139**, 99 (1997).
67. K. Dabov, A. Foi, V. Katkovnik, K. Egiazarian, *IEEE Trans. Image Process.* **16**, 2080 (2007).
68. R.A. Crowther, L.A. Amos, J.T. Finch, D.J. De Rosier, A. Klug, *Nature* **226**, 421 (1970).
69. Y. Liu, P.A. Penczek, B.F. McEwen, J. Frank, *Ultramicroscopy* **58**, 393 (1995).
70. R.F. Egerton, P. Li, M. Malac, *Micron.* **35**, 399 (2004).
71. J. Frank, *Three-Dimensional Electron Microscopy of Macromolecular Assemblies* (Oxford University Press, New York, 2006).
72. R. Gordon, R. Bender, G.T. Herman, *J. Theor. Biol.* **29**, 471 (1970).
73. A.H. Andersen, A.C. Kak, *Ultrason. Imaging* **6**, 81 (1984).
74. J. Miao, F. Förster, O. Levi, *Phys. Rev. B* **72**, 052103 (2005).
75. A. Pryor, Y. Yang, A. Rana, M. Gallagher-Jones, J. Zhou, Y.H. Lo, G. Melinte, W. Chiu, J.A. Rodriguez, J. Miao, *Sci. Rep.* **7**, 10409 (2017).
76. Y.H. Lo, C.-T. Liao, J. Zhou, A. Rana, C.S. Bevis, G. Gui, B. Enders, K.M. Cannon, Y.-S. Yu, R. Celestre, K. Nowrouzi, D. Shapiro, H. Kapteyn, R. Falcone, C. Bennett, M. Murnane, J. Miao, *Sci. Adv.* **5**, eaax3009 (2019).
77. G. Haberfehlner, P. Thaler, D. Knez, A. Volk, F. Hofer, W.E. Ernst, G. Kothleitner, *Nat. Commun.* **6**, 8779 (2015).

78. J. Park, H. Elmlund, P. Ercius, J.M. Yuk, D.T. Limmer, Q. Chen, K. Kim, S.H. Han, D.A. Weitz, A. Zettl, A.P. Alivisatos, *Science* **349**, 290 (2015).
79. H. Yang, R.N. Rutte, L. Jones, M. Simson, R. Sagawa, H. Ryll, M. Huth, T.J. Pennycook, M.L.H. Green, H. Soltau, Y. Kondo, B.G. Davis, P.D. Nellist, *Nat. Commun.* **7**, 12532 (2016).
80. S. Gao, P. Wang, F. Zhang, G.T. Martinez, P.D. Nellist, X. Pan, A.I. Kirkland, *Nat. Commun.* **8**, 163 (2017).
81. Y. Jiang, Z. Chen, Y. Han, P. Deb, H. Gao, S. Xie, P. Purohit, M.W. Tate, J. Park, S.M. Gruner, V. Elser, D.A. Muller, *Nature* **559**, 343 (2018).
82. D.A. Muller, L.F. Kourkoutis, M. Murfitt, J.H. Song, H.Y. Hwang, J. Silcox, N. Dellby, O.L. Krivanek, *Science* **319**, 1073 (2008).
83. Q. Ding, Y. Zhang, X. Chen, X. Fu, D. Chen, S. Chen, L. Gu, F. Wei, H. Bei, Y. Gao, M. Wen, J. Li, Z. Zhang, T. Zhu, R.O. Ritchie, Q. Yu, *Nature* **574**, 223 (2019).
84. H. Yang, L. Jones, H. Ryll, M. Simson, H. Soltau, Y. Kondo, R. Sagawa, H. Banba, I. MacLaren, P.D. Nellist, *J. Phys. Conf. Ser.* **644**, 012032 (2015).
85. W. Gao, C. Addiego, H. Wang, X. Yan, Y. Hou, D. Ji, C. Heikes, Y. Zhang, L. Li, H. Huyan, T. Blum, T. Aoki, Y. Nie, D. Schlom, R. Wu, X. Pan, *Nature* **575**, 480 (2019).
86. C. Ophus, J. Ciston, J. Pierce, T.R. Harvey, J. Chess, B.J. McMorran, C. Czarnik, H.H. Rose, P. Ercius, *Nat. Commun.* **7**, 10719 (2016).
87. D. Zhang, Y. Zhu, L. Liu, X. Ying, C.-E. Hsiung, R. Sougrat, K. Li, Y. Han, *Science* **359**, 675 (2018).
88. Y. Li, Y. Li, A. Pei, K. Yan, Y. Sun, C.-L. Wu, L.-M. Joubert, R. Chin, A.L. Koh, Y. Yu, J. Perrino, B. Butz, S. Chu, Y. Cui, *Science* **358**, 506 (2017).
89. M.J. Zachman, Z. Tu, S. Choudhury, L.A. Archer, L.F. Kourkoutis, *Nature* **560**, 345 (2018).
90. H. Yoshida, Y. Kuwauchi, J.R. Jinschek, K. Sun, S. Tanaka, M. Kohyama, S. Shimada, M. Haruta, S. Takeda, *Science* **335**, 317 (2012).
91. H.-G. Liao, L. Cui, S. Whitelam, H. Zheng, *Science* **336**, 1011 (2012).
92. X. Tian, D.S. Kim, S. Yang, C.J. Ciccarino, Y. Gong, Yo. Yang, Ya. Yang, B. Duschatko, Y. Yuan, P.M. Ajayan, J.C. Idrobo, P. Narang, J. Miao, *Nat. Mater.*, https://doi.org/10.1038/s41563-020-0636-5 (2020).
93. D. Ren, C. Ophus, M. Chen, L. Waller, *Ultramicroscopy* **208**, 112860 (2020). □

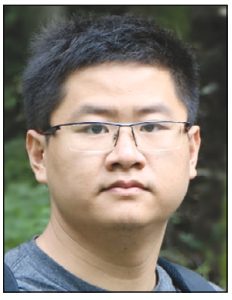

Jihan Zhou is an assistant project scientist of physics and astronomy at the University of California, Los Angeles (UCLA). He received his bachelor's degree in chemistry and his PhD degree in polymer chemistry and physics from Peking University, China, in 2009 and 2014, respectively. He completed postdoctoral research at UCLA, performing the first four-dimensional atomic electron tomography experiment on capturing early-stage nucleation. His research focuses on using and developing advanced electron microscopy and atomic electron tomography to solve traditionally intractable problems in chemistry, physics, materials science, and nanoscience at the atomic level. Zhou can be reached by email at jihan.zhou@physics.ucla.edu.

Yongsoo Yang is an assistant professor in the Department of Physics at the Korea Advanced Institute of Science and Technology (KAIST), Republic of Korea. He received his bachelor's degree in physics and mathematical science from Seoul National University, Republic of Korea in 2009, and his PhD degree in physics from the University of Michigan in 2014. He completed postdoctoral research at UCLA. His research focuses on structural determination beyond conventional crystallography, to resolve multidimensional (e.g., three dimensions + time, temperature, external field) atomic structure of materials with surface/interface or defects where perfect crystal symmetry is broken. Yang can be reached by email at yongsoo.yang@kaist.ac.kr.

Peter Ercius is a staff scientist at the National Center for Electron Microscopy (NCEM) facility within the Molecular Foundry Division at Lawrence Berkeley National Laboratory. He received his BSc and PhD degrees at Cornell University from the Applied and Engineering Physics Department in 2003 and 2009, respectively. He completed postdoctoral research at NCEM. His research focuses on the electron tomography program at NCEM using the TEAM 0.5 aberration-corrected instrument, atomic-resolution electron tomography, scanning nanodiffraction, *in situ* liquid cell electron microscopy, and two-dimensional/three-dimensional image analysis. Ercius can be reached by email at percius@lbl.gov.

Jianwei (John) Miao is a professor of physics and astronomy at the University of California, Los Angeles. He received his MS degree from the Chinese Academy of Sciences in 1994 and his PhD degree in physics from Stony Brook University, The State University of New York, in 1999. As a graduate student, he performed a seminal experiment of extending x-ray crystallography to allow structural determination of noncrystalline specimens, known as coherent diffractive imaging (CDI), lensless imaging or computational microscopy. CDI methods such as plane-wave CDI, Bragg CDI, and ptychography have been broadly implemented using synchrotron radiation, x-ray free electron lasers, high harmonic generation, optical lasers, and electrons. He also pioneered atomic electron tomography (AET) and recently led a team that developed four-dimensional AET to observe crystal nucleation at atomic resolution for the first time. Miao can be reached by email at miao@physics.ucla.edu.